Viscoplastic fingers and fractures in a Hele-Shaw cell

Thomasina V. Ball[a,*], Neil J. Balmforth[a], Ariel P. Dufresne[a]

[a] *Department of Mathematics, University of British Columbia, Vancouver, BC, V6T 1Z2, Canada*

Abstract

A study is presented of the instabilities that may arise in radial displacement flows of yield-stress fluid in a Hele-Shaw cell. Theoretically, the viscoplastic version of the Saffman-Taylor interfacial instability is predicted to arise when the yield-stress fluid is displaced by a Newtonian one. The interface is expected to remain stable, however, if the yield-stress fluid displaces the Newtonian one. A variety of experiments are then performed using an aqueous suspension of Carbopol. As predicted theoretically, the Saffman-Taylor instability is observed when the Carbopol is displaced by either air or an immiscible oil, and no instabilities are observed when the displacement is the other way around. However, when water is used in the displacement experiments, other instabilities appear that take the form of localized fractures of the Carbopol over the sections of the interface that are under tension. The fractures arise in both the stable and unstable Saffman-Taylor configurations, leading to a rich range of patterns within the Hele-Shaw cell. We argue that this pattern formation cannot be explained by a recently proposed instability of shear-thinning extensional flow, whatever the degree of effective slip over the plates of the cell. Instead, we attribute the fractures to a reduction in the fracture energy of the suspension when placed in contact with water.

1. Introduction

The so-called Saffman-Taylor instability [1] is well-known to lead to labyrinthian fingering patterns when a viscous fluid emplaced in a narrow conduit is displaced by a second, less viscous fluid. The simplest visualization of this phenomenon is provided by emplacing the more viscous fluid in a thin rectangular slot, or Hele-Shaw cell, and then (radially) pumping in the second fluid [2, 3, 4], or simply pulling apart the walls allowing air to displace the fluid interface (a popular device that has found its way into art installations). This type of fingering instability has also been studied for complex fluids, including both visco-elastic liquids [5, 6] and yield-stress fluids [7, 8, 9, 10, 11, 12, 13, 14, 15, 16], with potential applications to oil extraction from porous media in the petroleum industry.

In the present study, we undertake an experimental exploration of the fingering patterns created by viscoplastic radial displacement flows in a Hele-Shaw cell. We consider both the Saffman-Taylor configuration, to examine the viscoplastic version of classical fingering, and its inverse, which is expected theoretically to be stable. We preface our discussion with theoretical background, providing details of the viscoplastic Saffman-Taylor problem and advancing beyond previous work [7, 11]. In particular, we treat the stability problem as an initial-value problem, which is necessary when the base state of axisymmetrical expansion is time-dependent (as for radial displacements) and a normal-mode-type approach is not strictly valid. We further explicitly consider two types of unstable displacements that can be set up in the laboratory, both sketched in figure 1: the extraction of a disk and the expansion of an annulus of viscoplastic fluid. The stable configuration expected for an emplaced viscoplastic disk provides a third type of displacement that we consider (figure 1(a)).

In our experiments, the working fluids are mainly aqueous suspensions of Carbopol in combination with either air or water. We expose a rich variety of patterns that form in the displacement flows, many of which are **not** driven by instabilities of the Saffman-Taylor flow variety (see figure 1). Instead, we argue that the Carbopol gel actually fractures in a solid-like manner when the interface is in contact with water and under tension. This leads to a rich range of fracturing patterns. Only when we use either air or an immiscible liquid does the Carbopol resist fracture and the conventional Saffman-Taylor instability appear.

Visco-elastic fracture has previously been suggested to arise in displacement flows of other complex fluids in Hele-Shaw cells [17, 18, 19, 9, 20]. However, this was claimed to develop as a natural variation on the Saffman-Taylor theme, with no critical dependence on whether the second fluid is water-based (although van Damme *et al.* point out the significance of whether the materials are miscible or not). By contrast, for our Carbopol suspensions, we show that the fracturing is definitely distinct from Saffman-Taylor-type fingering and is critically sensitive to the presence of water at the interface, along similar lines to a number of other problems [21, 22, 23].

We also consider, and dismiss, an entirely different

*Corresponding author: *E-mail:* tvball@math.ubc.ca, *Telephone:* 604 827 3034

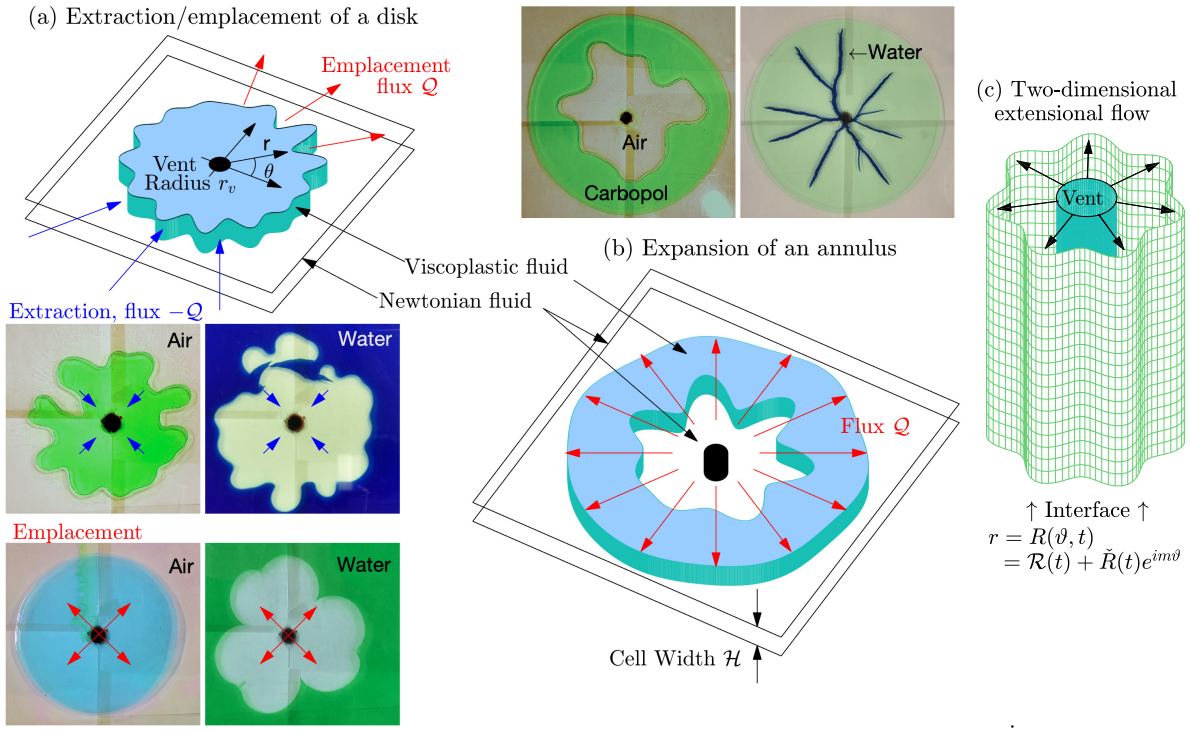

Figure 1: Sketches of (a) an extracted or emplaced viscoplastic disk, (b) an expanding viscoplastic annulus and (c) two-dimensional extensional flow. For (a) and (b), images from our experiments are inset to illustrate the variety of observed non-axisymmetrical patterns. With air, the retreating interfaces of the viscoplastic disk and annulus suffer a variant of the Saffman-Taylor instability; the advancing interface remains stable. Using water, fractures appear that sever the Saffman-Taylor fingers of the extracted disk, and create a flower-like and dendritic patterns for the expanding disk and annulus. The vent is visible as the black disk at the centre of the images; the faint grey lines reveal the overlapping edges of paper attached to the underside of the lower (transparent) plate of the cell. The fluids are dyed various shades of green and blue (using food dye or ink) to help visualize the interfaces.

mechanism that may destabilize extensional flows of viscoplastic fluid [24, 25]: Sayag & Worster demonstrated that an expanding cylinder of power-law fluid is unstable to non-axisymmerical perturbations if sufficiently shear thinning (as illustrated in figure 1(c)). However, this instablity is two-dimensional and is not necessarily expected in a Hele-Shaw cell where the fluid is narrowly confined between two walls and shears substantially across the cell when no-slip conditions hold on the plates. Nevertheless, complex fluids are also well known to experience significant effective slip [26]. Should that slip become extreme, and the fluid slide freely over the walls, the flow dynamics of the Hele-Shaw cell become more closely two-dimensional. In this setting, the extensional flow instability of Sayag & Worster may play a role. Indeed, it has been suggested previously that sliding prompted by effective slip may be responsible for the development of weakly non-axisymmetrical patterns in gravity currents of Carbopol [27]. With this in mind, we reconsider the theoretical analysis of Sayag & Worster for a yield-stress fluid (Appendix A; figure 1(c)). That analysis suggests that the instability is relatively weak under the conditions of our experiments and unlikely to explain the fracture patterns we observe in stable Saffman-Taylor configurations. In fact, wall slip, though observed for Carbopol under similar conditions as those for our experiments, is typically only a small fraction of the bulk flow speed [28].

2. Theoretical background

We consider a Herschel-Bulkley fluid with consistency K, power-law index n and yield stress τ_Y. The fluid is pumped into or out of a Hele-Shaw cell of thickness $\mathcal{H}$, with flux $\pm\mathcal{Q}$ through a central hole of radius r_v. We use the cylindrical polar coordinates (r, ϑ, z) to describe the geometry, with $z = 0$ representing the midplane of the cell; see figure 1.

2.1. Reduced model

Following classical theory for a Hele-Shaw cell [29], the slot-averaged flux $\mathbf{q}$ satisfies

$$\boldsymbol{\nabla} \cdot \mathbf{q} = 0, \qquad \mathbf{q} = -\frac{Q(S; \mathrm{Bi}, n)}{S} \boldsymbol{\nabla} p, \tag{1}$$

where $S = |\boldsymbol{\nabla} p|$, the in-plane gradient operator is $\boldsymbol{\nabla}$, and the flux function,

$$Q = \frac{1}{n+1} (1 - Y)_+^{1+\frac{1}{n}} (n + 1 + nY) S^{\frac{1}{n}}, \tag{2}$$

with

$$Y = \frac{\mathrm{Bi}}{S}, \qquad (1-Y)_+ \equiv \mathrm{Max}(1-Y, 0). \tag{3}$$

To arrive at this dimensionless model, the characteristic lengthscale scale $\mathcal{L} = r_v$ is used to scale distances in the plane of the Hele-Shaw cell (*i.e.* the radial coordinate r), and the cell half-thickness $\frac{1}{2}\mathcal{H}$ for z. The velocity and time scales are $\mathcal{V} = \mathcal{Q}/(2\pi\mathcal{L}\mathcal{H})$ and $\mathcal{L}/\mathcal{V}$. The pressure p is scaled by $12\mu_*\mathcal{V}\mathcal{L}/\mathcal{H}^2$, where $\mu_* = \frac{1}{3}K(2+\frac{1}{n})^n(2\mathcal{V}/\mathcal{H})^{n-1}$. The dimensionless yield stress, or Bingham number, is

$$\mathrm{Bi} = \frac{\tau_Y\mathcal{H}}{6\mu_*\mathcal{V}}. \tag{4}$$

In the analysis leading to (1)–(2), the shear stresses across the slot (τ_{rz} and $\tau_{z\theta}$) provide the main resistance to the flow driven by the pressure gradient, establishing a characteristic flow profile across the gap. Provided $Y < 1$, that profile consists of fully sheared layers adjacent to the walls of the cell, sandwiching a central plug-like flow over $-Y < z < Y$; if Y reaches unity (the dimensionless wall position), the plug-like layer fills the gap to form a rigid blockage.

The flux-pressure-gradient relation (2) is illustrated in figure 2 and has two key limits: for $\mathrm{Bi} \to 0$, $Q \to S^{\frac{1}{n}}$, corresponding to the limit of a power-law fluid. In addition, if $n = 1$, $Q \to S$ and (1) reduces to Laplace's equation, in the usual manner of viscous Hele-Shaw flow. For $\mathrm{Bi} \gg 1$, $Q \to (2n+1)(1-Y)^{1+\frac{1}{n}}\mathrm{Bi}^{\frac{1}{n}}/(n+1)$, which demands that $S = O(\mathrm{Bi})$ and $Y \to 1$. This limit corresponds to a perfectly plastic material with a specific sliding law applying at the walls dictated by the yielded boundary layers that remain there.

Experimentally, one can conveniently set up a configuration susceptible to Saffman-Taylor fingering by extracting a disk of yield-stress fluid from the cell, with either air or another Newtonian fluid with relatively small viscosity on the outside (figure 1(a)). Conversely, when the yield-stress fluid is pumped into the cell to emplace a viscoplastic disk, the interface is expected to remain stable. To explore either situation theoretically, we consider a viscoplastic disk with edge located at $r = R(\vartheta, t)$ satisfying the kinematic condition,

$$\left(\frac{\partial}{\partial t} + \frac{\mathbf{q}\cdot\hat{\boldsymbol{\vartheta}}}{r}\frac{\partial}{\partial\vartheta}\right)R = \mathbf{q}\cdot\hat{\mathbf{r}} \qquad \text{at } r = R. \tag{5}$$

We can also set up another arrangement to study the viscoplastic version of Saffman-Taylor fingering by first pumping viscoplastic fluid within the cell, and then switching the feeder tube to pump in a second Newtonian fluid. This creates an expanding annulus of viscoplastic fluid for which the outer interface remains stable but the inner edge may lose axisymmetry and develop fingers (figure 1(b); *cf.* [30]). Kinematic conditions of the form (5) then apply at the inner and outer edges of the annulus located at $r = R_{_I}(\vartheta, t)$ and $r = R_{_O}(\vartheta, t)$.

For a given flux and at comparable radii, the instantaneous growth rate of disturbances to an unstable interface is not expected to be very different between these two scenarios. However, for the extracted disk, the unstable interface has an compressive hoop stress. Conversely, for the expanding annulus, the unstable inner interface has a hoop stress ($\tau_{\theta\theta}$) that is tensile. We return later to this important difference.

For either scenario, the mathematical formulation is closed by applying pressure conditions at the interfaces. To simplify this task, we ignore the pressure drops arising from the viscous resistance of the Newtonian fluid surrounding the viscoplastic disk or annulus, and assume that the interfaces have no curvature across the cell. The pressure conditions are then $p = \kappa\mathcal{K}[R]$ at $r = R$ for the disk, and

$$p = \begin{cases} P_{in} - \kappa_{_I}\mathcal{K}[R_{_I}], & r = R_{_I}, \\ \kappa_{_O}\mathcal{K}[R_{_O}], & r = R_{_O}, \end{cases} \tag{6}$$

for the annulus. Here, P_{in} denotes the inlet pressure, the curvature of each interface is given by

$$\mathcal{K}[R] = \frac{R^2 + 2(\partial R/\partial\vartheta)^2 - R\partial^2 R/\partial\vartheta^2}{[R^2 + (\partial R/\partial\vartheta)^2]^{\frac{3}{2}}} \tag{7}$$

(*cf.* [4]), and $(\kappa, \kappa_{_I}, \kappa_{_O})$ denote dimensionless interfacial tensions parameters (the dimensional tensions scaled by $\mathcal{H}^2/(12\mu_*\mathcal{V}\mathcal{L}^2)$).

2.2. Axisymmetrical flow

When the net dimensionless flux is constant and equal to 2π, an axisymmetrical flow is possible, driven by a local radial pressure gradient, $S \to \mathcal{S}(r, t)$, satisfying the algebraic relation,

$$\frac{1}{r} = Q(\mathcal{S}; n, \mathrm{Bi}). \tag{8}$$

For an expanding disk, the flux is directed outwards and the background pressure gradient is negative; for an extracted disk, the flux is directed inwards and the background pressure gradient is positive. The single interface is therefore at

$$r = \mathcal{R}(t) = \sqrt{R_{_A}^2 - 2\sigma t}, \tag{9}$$

where $R_{_A}$ denotes its initial position and $\sigma = \mp 1$ identifies an advancing or retreating interface, respectively. For the expanding annulus, the pressure gradient is necessarily negative; the corresponding circular fluid edges are

$$\begin{aligned} R_{_I}(t) &= \sqrt{1+2t} \equiv \mathcal{R}_{_I}(t), \\ R_{_O}(t) &= \sqrt{R_{_A}^2 + 2t} \equiv \mathcal{R}_{_O}(t), \end{aligned} \tag{10}$$

where $R_{_A}$ is now the initial outer radius.

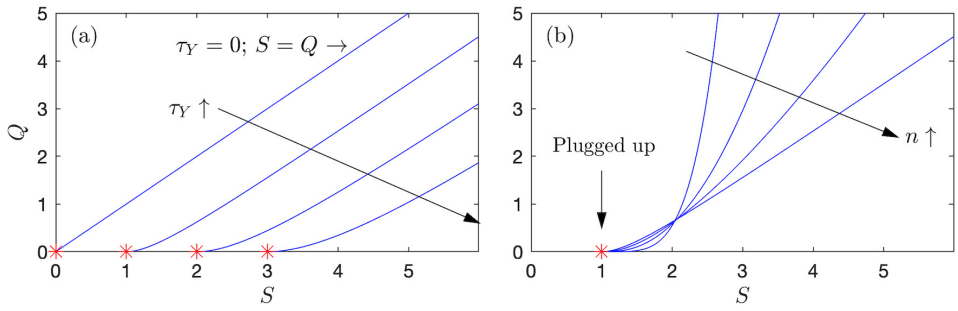

Figure 2: Flux functions for different (a) Bingham numbers $\mathrm{Bi} = 0$, 1, 2 and 3 (with $n = 1$) and (b) different power-law exponents $n = \frac{1}{4}$, $\frac{1}{2}$, $\frac{3}{4}$ and 1 (with $\mathrm{Bi} = 1$).

2.3. Linear stability

Linear non-axisymmetrical perturbations, with dependence $e^{im\vartheta}$ and a pressure distinguished by a hat decoration, satisfy

$$\frac{1}{r}\frac{\partial}{\partial r}\left(rQ'\frac{\partial \hat{p}}{\partial r}\right) = \frac{m^2\hat{p}}{r^2\mathcal{S}}Q(\mathcal{S};n,\mathrm{Bi}) \equiv \frac{m^2\hat{p}}{r^3\mathcal{S}}, \tag{11}$$

where

$$Q' = \frac{1}{r}\left[\frac{(n+1)}{(n+1)\mathcal{S}+n\mathrm{Bi}} + \frac{(n+1)}{n(\mathcal{S}-\mathrm{Bi})} - \frac{2}{\mathcal{S}}\right]. \tag{12}$$

2.3.1. Planar instability

We may recover the viscoplastic version of the Saffman-Taylor instability for a single planar interface from (11) by switching radial derivatives for Cartesian ones, replacing the left-hand side by $Q'\hat{p}_{xx}$, and introducing the planar transverse wavenumber $\ell \equiv m/r$ on the right. The interface, now at $x = \mathcal{X} + \hat{X}(t)e^{i\ell y}$, travels at a fixed speed under a constant pressure gradient of magnitude $\mathcal{S}$ in the absence of the transverse perturbations with amplitude $\hat{X}(t)$. We take the viscoplastic fluid to lie to the left of the interface; when that fluid is advancing, the interface moves to the right with a speed Q and the pressure gradient is $-\mathcal{S}$; in retreat, the interface moves left with speed $-Q$ under a pressure gradient $\mathcal{S}$. Thence,

$$\frac{\partial^2\hat{p}}{\partial x^2} = \frac{\ell^2 Q}{\mathcal{S}Q'}\hat{p}, \tag{13}$$

or

$$\hat{p} = -(\sigma\mathcal{S} - \kappa\ell^2)\hat{X}\exp\left(i\ell y + |\ell|\sqrt{\frac{Q}{\mathcal{S}Q'}}|x-\mathcal{X}|\right), \tag{14}$$

after linearizing about the undisturbed position of the interface, $x = \mathcal{X}$, given that the pressure condition there becomes $\hat{p} + \sigma\mathcal{S}\hat{X}e^{i\ell y} = \kappa\ell^2\hat{X}e^{i\ell y}$, where $\sigma = \mp 1$ again distinguishes the cases of an advancing or retreating interface (*i.e.* the sign of the background pressure gradient). The linearized kinematic condition, $\hat{X}_t = -Q'\hat{p}_x$, now gives

$$\frac{\mathrm{d}\hat{X}}{\mathrm{d}t} = |\ell|\sqrt{\frac{QQ'}{\mathcal{S}}}(\sigma\mathcal{S} - \kappa\ell^2)\hat{X}. \tag{15}$$

The retreating interface is therefore unstable to transverse perturbations with wavenumbers $|\ell| < \sqrt{\mathcal{S}/\kappa}$, with the wavelength of maximum growth given by $2\pi/\ell = 2\pi\sqrt{3\kappa/\mathcal{S}}$. Notably, because one must exceed a threshold pressure gradient for force flow, $\mathcal{S}$ remains finite for $Q \to 0$, and so the most unstable wavelength remains finite in the limit that the flow rate ceases (for finite interfacial tension), in contrast to the viscous version of the problem (*cf.* [7, 8]). In particular, in dimensional terms and the perfectly plastic limit ($\mathcal{S} \to \mathrm{Bi}$), the most unstable wavelength is $2\pi\mathcal{L}\sqrt{3\kappa/\mathrm{Bi}} = \pi\sqrt{6\mathcal{H}\gamma/\tau_Y}$. Note that the growth rate implied by (15) is a little different from that presented by [7] because we avoid any approximation of the flux-pressure-gradient relation in (2) (similarly the results for radial flow with a single interface are also slightly different from those presented by both [7] and [11]).

2.3.2. An expanding or extracting viscoplastic disk

For the disk, we write the disturbed interface position and pressure as $R(\vartheta,t) = \mathcal{R}(t) + \hat{R}(t)e^{im\vartheta}$ and $\hat{p} = \hat{p}^A(r,t)e^{im\vartheta}$. The linear perturbations satisfy (11) subject to the boundary conditions,

$$\hat{p}^A_r(1,t) = 0 \quad \& \quad \hat{p}^A(\mathcal{R},t) = (m^2-1)\frac{\kappa}{\mathcal{R}^2} - \sigma\mathcal{S}(\mathcal{R}), \tag{16}$$

which correspond to specifying the flux at the vent $r = 1$ and linearing the outer pressure condition around the position of the undisturbed interface. The similarly linearized kinematic condition then provides the instantaneous growth rate,

$$\hat{R}^{-1}\frac{\mathrm{d}\hat{R}}{\mathrm{d}t} = -[Q'\hat{p}^A_r]_{r=\mathcal{R}} - \frac{1}{\mathcal{R}^2}. \tag{17}$$

We may extract a stability condition directly from (17) as follows: by multiplying (11) by $\hat{p}^A$ and rearranging, it follows that $\hat{p}^A\hat{p}^A_r > 0$, in view of the pressure condition at the vent in (16). But $Q' > 0$ (see figure 2), and so the sign of $[Q'\hat{p}^A_r]_{r=\mathcal{R}}$ is given by that of $p^A(\mathcal{R},t)$ in (16). Thus, the interface is stable when $\sigma = -1$ (implying $p^A(\mathcal{R},t) > 0$ and therefore $[Q'\hat{p}^A_r]_{r=\mathcal{R}} > 0$) and can only be unstable if $\sigma = +1$. In other words, the advancing interface (emplaced disk) is stable, but the retreating interface (extracted disk) may be unstable.

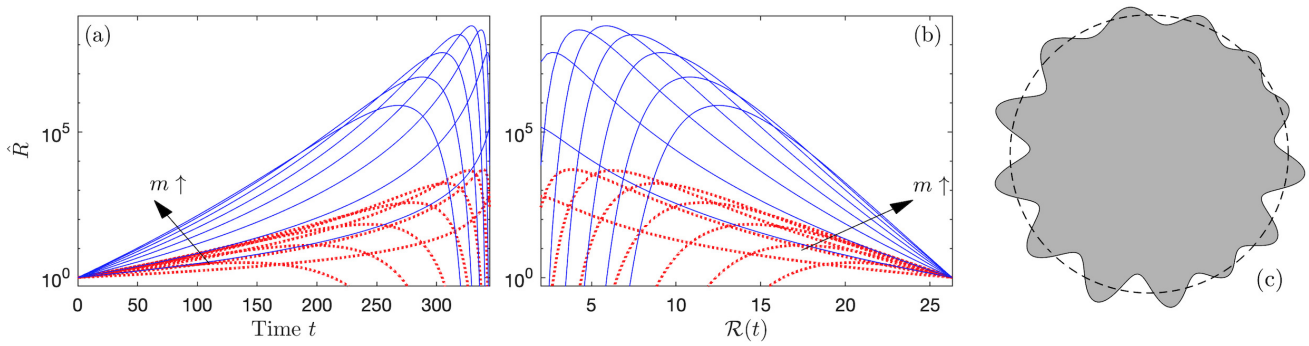

Figure 3: Interface perturbation amplitude $\hat{R}(t)$ for an extracted disk with $R_{_A} = 26.3$, $m = 2, 4, ..., 16$, Bi $= 0.38$, $n = 0.38$ and $\kappa = 0.5$, taking $\mathcal{H} = 1.7$mm, $\mathcal{Q} = 22$ml/min, $\mathcal{L} = r_v = 3.8$mm, and initial radius of 10cm (experimental parameters of §3.1). In (a), the amplitudes are plotted against time; $\hat{R}(t)$ is plotted against $\mathcal{R}(t)$ in (b). The dashed (red) lines show the corresponding results for Bi $= 0$. The shape of the interface when the mean radius is about $\frac{1}{2}R_{_A}$ is shown in (c), assuming a linear superposition of the modes $m = 1, 2, ..., 16$ with random phases and initial amplitudes of $O(10^{-7}\mathcal{L})$.

For the extraction of a Newtonian disk, the pressure solution is given by

$$\hat{p} \to \frac{(r^m + r^{-m})[(m^2-1)\kappa - \mathcal{R}]\hat{R}e^{im\vartheta}}{\mathcal{R}^2(\mathcal{R}^m + \mathcal{R}^{-m})},$$

leading to the instantaneous growth rate,

$$\hat{R}^{-1}\frac{\mathrm{d}\hat{R}}{\mathrm{d}t} = \frac{(m\mathcal{R}^{2m} - m - 1)}{\mathcal{R}^3(\mathcal{R}^{2m}+1)}[\mathcal{R} - (m^2-1)\kappa] - \frac{1}{\mathcal{R}^2}. \quad (18)$$

For a relatively small vent, $\mathcal{R} \gg 1$ and we recover the growth rate, $(m-1)[1 - m(m+1)\kappa/\mathcal{R}]/\mathcal{R}^2$, derived by Wilson [4] and Paterson [2].

In the opposite limit of large yield stress, Bi $\gg 1$, and taking $\kappa = O(\mathrm{Bi})$, we find

$$\hat{p} \sim \left[(m^2-1)\frac{\kappa}{\mathcal{R}^2} - \mathrm{Bi}\right]\hat{R}e^{im\vartheta} \times \left\{1 + m^2(nr+1)\left[\frac{(n+1)^n}{(2n+1)^n r^n \mathrm{Bi}}\right]^{\frac{1}{(n+1)}}\right\}. \quad (19)$$

The instantaneous growth rate is then

$$\hat{R}^{-1}\frac{\mathrm{d}\hat{R}}{\mathrm{d}t} \sim \frac{m^2}{\mathcal{R}^2}(\mathcal{R}-1)\left[1 - (m^2-1)\frac{\kappa}{\mathcal{R}^2}\right]. \quad (20)$$

Both (18) and (20) highlight the important role of surface tension in regularizing the Saffman-Taylor instability.

Numerical solutions for an extracted disk are shown in figure 3 for $n = \mathrm{Bi} = 0.38$, parameter settings that are guided by the experiments of §3.1 (*cf.* figures 5 and 6). At smaller times (larger radii), the effect of interfacial tension (parametrized here by setting $\kappa = 0.5$) is relatively low, leaving the higher wavenumber modes as the most unstable. That tension grows in importance due to the increasing curvature of the interface as the disk shrinks, gradually stabilizing the higher$-m$ modes and promoting the importance of the lower angular wavenumbers. For the parameters chosen, the most unstable modes have $m = 11$ or 12 when the mean radius of the interface is about half of its initial value. This is illustrated further in figure 3(c), which shows a sample pattern created by formulating a linear superposition of the first sixteen angular modes with equal initial amplitudes of $10^{-7}\mathcal{L}$ and random phases. For comparison, we note that the most unstable wavenumber of the planar instability problem implies a dominant angular wavenumber of $m \equiv \ell\mathcal{R} = \mathcal{R}\sqrt{\mathcal{S}/3\kappa}$. At the end of the computation, this provides a useful, if quantitatively inaccurate, estimate of $m \approx 15.0$.

Figure 3 also includes solutions for Bi $= 0$, which amplify less quickly than those for Bi > 0. This observation is in line with the expectation that the viscoplastic problem is more unstable than the Newtonian one because of its higher effective viscosity contrast across the interface.

2.3.3. An expanding viscoplastic annulus

For the annulus, the linearized pressure conditions demand that

$$\hat{p} = \begin{cases} [\mathcal{S} - \kappa_{_I}(m^2-1)/r^2]\hat{R}_{_I}e^{im\vartheta}, & r = \mathcal{R}_{_I}, \\ [\mathcal{S} + \kappa_{_O}(m^2-1)/r^2]\hat{R}_{_O}e^{im\vartheta}, & r = \mathcal{R}_{_O}, \end{cases} \quad (21)$$

where $\hat{R}_{_I}(t)e^{im\vartheta}$ and $\hat{R}_{_O}(t)e^{im\vartheta}$ denote the shifts to the inner and outer edges. We may therefore find two solutions to (11), $\hat{p}^{_I}(r,t)e^{im\vartheta}$ and $\hat{p}^{_O}(r,t)e^{im\vartheta}$, satisfying the conditions,

$$\hat{p}^{_I} = \begin{cases} \mathcal{S} - \kappa_{_I}(m^2-1)/r^2 & \text{at } r = \mathcal{R}_{_I} \\ 0 & \text{at } r = \mathcal{R}_{_O} \end{cases} \quad (22)$$

and

$$\hat{p}^{_O} = \begin{cases} 0 & \text{at } r = \mathcal{R}_{_I} \\ \mathcal{S} + \kappa_{_O}(m^2-1)/r^2 & \text{at } r = \mathcal{R}_{_O} \end{cases}. \quad (23)$$

The desired linear solution is then,

$$\hat{p} = [\hat{R}_{_I}(t)\hat{p}^{_I}(r,t) + \hat{R}_{_O}(t)\hat{p}^{_O}(r,t)]e^{im\vartheta}.$$

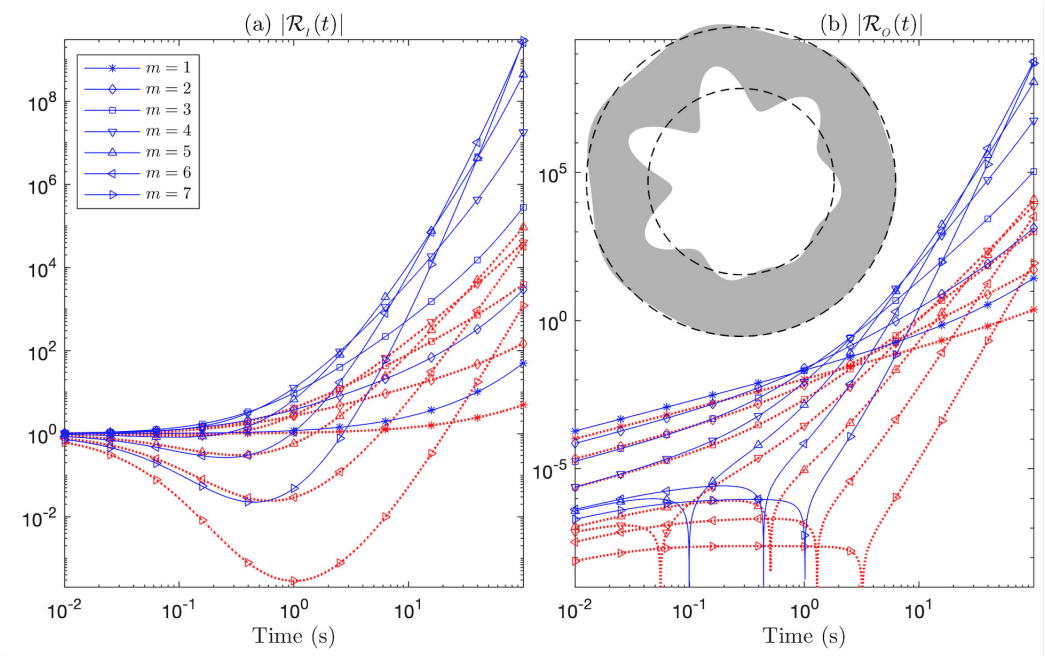

Figure 4: Numerical solutions for an expanding annulus, showing (a) $|\hat{R}_I(t)|$ and (b) $|\hat{R}_O(t)|$ for $m = 1$, 2, ..., 7, starting from the initial conditions $\hat{R}_I(0) = 1$ and $\hat{R}_O(0) = 0$, with Bi = 0.39 (blue, solid lines) and Bi = 0 (red dotted lines), and $n = 0.38$. Times are shown in seconds, taking $\mathcal{H} = 1.7$mm, $\mathcal{Q} = 20$ml/min, and $\mathcal{L} = r_v = 3.8$mm (experimental parameters of §3.1). Interfacial tension is included, assuming $\kappa_I = \kappa_O = 0.073$. The inset in (b) shows a snapshot of the final state, assuming that the different modes in m are linearly superposed and all initialized with amplitudes of $O(10^{-9}\mathcal{L})$ and random phases. The downward spikes in $|\hat{R}_O(t)|$ correspond to zero crossings.

The linearizations of the kinematic conditions now furnish the system

$$\frac{\mathrm{d}\hat{R}_I}{\mathrm{d}t} = -\left[(Q'\hat{p}_r^I + r^{-2})\hat{R}_I + Q'\hat{p}_r^O\hat{R}_O\right]_{r=\mathcal{R}_I}, \qquad (24)$$

$$\frac{\mathrm{d}\hat{R}_O}{\mathrm{d}t} = -\left[Q'\hat{p}_r^I\hat{R}_I + (Q'\hat{p}_r^O + r^{-2})\hat{R}_O\right]_{r=\mathcal{R}_O}. \qquad (25)$$

Numerical solutions of for $|\hat{R}_I(t)|$ and $|\hat{R}_O(t)|$ for an expanding annulus with $(n, \mathrm{Bi}) = (0.38, 0.39)$ and m = 1,2, ..., 7 are shown in figure 4, beginning with the initial conditions, $\hat{R}_I(0) = 1$ and $\hat{R}_O(0) = 0$. The choices for n and Bi are again values guided by the experiments in §3.1 (*cf.* figure 5), and interfacial tension is included at both edges, taking $\kappa_I = \kappa_O = 0.073$ (corresponding to adopting the surface tension of water for γ_O and γ_I). The interfacial tension stabilizes the higher modes at early time, but this effect declines as the edges expand and curvatures decrease, until all the modes begin to grow with rates that increase with m. This competition leaves the $m = 6$ mode as the strongest at the end of the computation (see figure 4(c)); the most unstable wavenumber of the corresponding planar problem suggests a dominant angular wavenumber of $m \equiv \ell\mathcal{R} \approx 9.8$. Once again, the Newtonian problem with Bi = 0 is less unstable.

3. Experiments

The theoretical analysis of §2 indicates that the retreating interfaces of an extracted disk and an expanding annulus of viscoplastic fluid suffer the viscoplastic version of the classical Saffman-Taylor instability. Conversely, the advancing interface of a expanding viscoplastic disk remains stable. Because the basic state of axisymmetrical expansion is time-dependent, the linear initial-value problem must be solved to determine which angular modes are the most unstable for a retreating interface, particularly because the changing curvature of the undisturbed interface impacts the stabilizing effect of surface tension. We now explore the experimental versions of these scenarios, paying particular attention to whether the Newtonian fluid is water.

The experiments involved pumping aqueous suspensions of Carbopol (Ultrez 20, with concentrations of between 0.15-0.45% by weight, and neutralized with sodium hydroxide) into or out of a cell made from plexiglass plates. Spacers between the plates furnishes cells with gaps of thickness ranging from 1.7mm to 4.3mm. We used fits to the flow curves obtained from a rheometer (Kinexus Malvern rheometer fitted with roughened parallel plates) to estimate Herschel-Bulkley parameters for the Carbopol solutions.

When the test was aimed at exploring the displacement of a Newtonian fluid by Carbopol, we pumped the gel into either an empty cell (so that the Carbopol displaced air), or first filled the gap with a viscous liquid. When the test demanded that we displace the gel, we began by pumping Carbopol into the cell to form a disk with a given radius. We then either reversed the pump to extract the Carbopol,

or switched the inlet pipe and pumped in a Newtonian fluid to create an expanding viscoplastic annulus. In the extraction tests, we either left the gap empty to study displacement by air, or surrounded the Carbopol with a displacing viscous liquid.

A first observation is that the Carbopol remains largely axisymmetrical when pumped into an empty (air-filled) cell (we show an example of this later in figure 14). Evidently, any imperfections in the surfaces and alignment of the walls are not sufficiently significant to desymmetrize the flow. Moreover, there is no sign that effective slip over the plexiglass plates precipitates the extensional flow instability described by Sayag & Worster (see Appendix A).

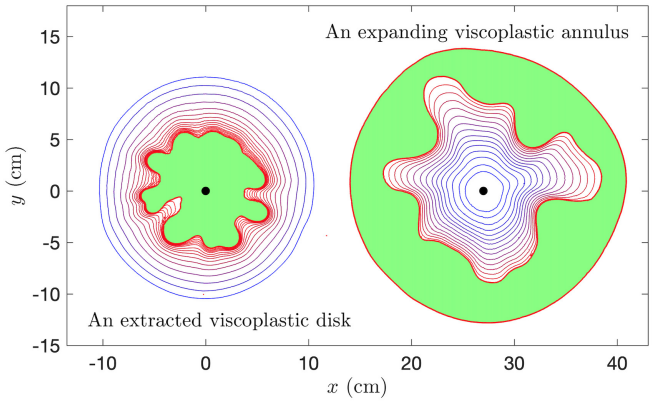

Figure 5: Experiments withdrawing a disk of Carbopol surrounded by air (left, flux $\mathcal{Q} \simeq 22$ml/min) or pumping air into an annulus of Carbopol (right, $\mathcal{Q} \simeq 20$ml/min). Shown are snapshots of the unstable interface, colour coded by time, with the final distribution of Carbopol shown shaded and the vent indicated by a small black disk. The initial Carbopol radius is about 10cm and the cell has thickness $\mathcal{H} = 1.7$mm; the rheology is $(n, \tau_Y, K) = (0.38, 22\text{Pa}, 13\text{Pa s}^n)$.

3.1. Viscoplastic Saffman-Taylor fingers

The displacement of Carbopol by air provides a convenient illustration of the viscoplastic analogue of classical Saffman-Taylor fingering. Our two versions of this problem are shown in figure 5. On the left side of figure 5, snapshots of the evolving, unstable interface are displayed when a disk of Carbopol in an air-filled cell is withdrawn through the vent. A finger pattern develops characterized by a distinctive set of angular modes; just before the strongest finger breaks through to the vent (which occurs when the average radius is about half the initial one), modes with $m = 12$ or so dominate the pattern. The second experiment, on the right of the picture, is a test when air is pumped into an annulus of Carbopol; the interface initially expands axisymmetrically, but then develops a non-axisymmetrical pattern, this time characterized by a lower angular wavenumber. At the end of the test, the pattern has dominant components with m around 7.

For the expanding annulus, there was little variability in the dominant wavenumbers when the flux was varied from $\mathcal{Q} \approx 10$ml/min upto 40ml/min or so. Moverover, similar results and patterns were found when we pumped immiscible Newtonian fluids into the cell instead of air. In particular, we used mineral spirits and a paraffin-based lamp oil, with viscosities comparable or slightly higher than that of water (about 1 or 3 mPa s, respectively), and tensions at an interface with water expected to be about half the surface tension of water in air.

The relatively weak fingering patterns observed in figure 5 are suggestive of Saffman-Taylor fingers controlled by a relatively strong interfacial tension. For the case of the expanding annulus, the most unstable wavenumber compares well with the result expected theoretically in §2.3.3 (see figure 4). The insensitivity of the dominant wavenumbers to the flux $\mathcal{Q}$ can also matched by theoretical computations. Despite this, for the extracted viscoplastic disk, experimental observations are only consistent with the theoretical expectations of §2.3.2, as shown in figure 3, if the surface tension parameter κ is taken to be seven times larger than expected, assuming the Carbopol has a surface tension comparable to water. The reason for this discrepancy is not clear.

Similar viscoplastic Saffman-Taylor fingering patterns to those in figure 5 are presented by [9] for radial displacement tests in thinner Hele-Shaw cells, and by [10, 14, 15, 16] for experiments in which the plates were pulled apart. However, the fingering is stronger and more labyrinthian in structure.

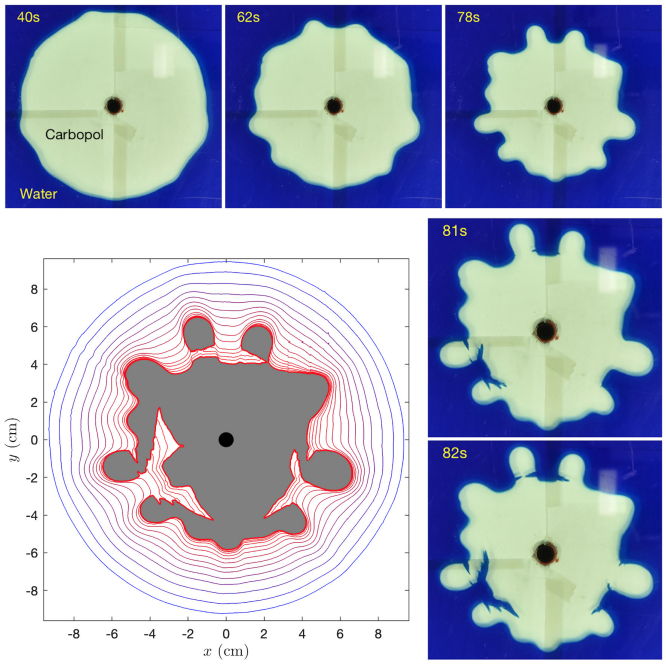

Figure 6: Withdrawal of Carbopol from a cell filled with blue-coloured water. (Pump rate $\mathcal{Q} \simeq 20$ml/min; gap $\mathcal{H} = 1.7$mm; rheology $(n, \tau_Y, K) = (0.38, 22\text{Pa}, 13\text{Pa s}^n)$. The images in the top row show the Saffman-Taylor-like pattern which develops relatively slowly; the lower images on the right display rapidly propagating fractures. In the main panel, the interface is plotted at a succession of times, with the colour representing time; the final distribution of Carbopol is shown shaded.

3.2. Fracture patterns

3.2.1. In extraction

When we repeat the extraction experiment (*i.e.* that on the left side of figure 5) with water filling the cell around the Carbopol, the water-Carbopol interface initially evolves much as in the air-displacement test: the interface shrinks around the vent, then suffers a mild fingering instability characterized by angular wavenumbers of $m = 12$ or so; see figure 6. Subsequently, however, a very different behaviour arises in which some of the concave sections of the interface abruptly tear apart, creating what appear to be fractures of the gel across the entire gap of the Hele-Shaw cell. These fractures then propagate rapidly into the gel at angles close to the azimuthal direction, rather than radially (the direction in which the Saffman-Taylor fingers typically break through to the vent at the end of an air-displacement test). The fractures thereby disfigure the fingering pattern, severing several of the Saffman-Taylor fingers and leaving a rather more complicated looking structure. The locations at which the fractures first form correspond to the positions along the interface with greatest concavity, suggestive of the areas with highest tensile stress. Thus, with water as the displacing fluid, the extraction experiment clearly shows a primary, weak Saffman-Taylor-type instability, followed by a secondary, but strong, tearing instability.

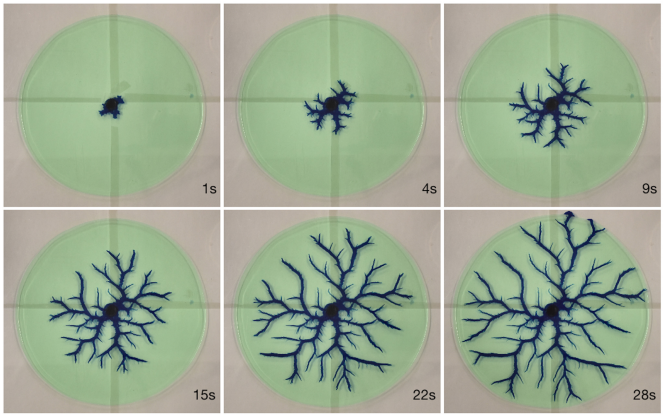

Figure 7: Blue-coloured water pumped into an annulus of (light green) Carbopol in a cell of thickness 3.3mm, with pump rate $\mathcal{Q} \simeq 40$ml/min. (Rheology: $n = 0.4$, $\tau_Y = 17$Pa, $K = 9.8$Pa s^n).

3.2.2. For a viscoplastic annulus

A similar fracture phenomenon arises when water is pumped into an annulus of Carbopol rather than air. Figures 7-9 display three such tests. The experiment in figure 7 shows the dendritic fracture network that arises from pumping blue-coloured water into a light-green disk of Carbopol. In this example, no weak Saffman-Taylor-like instability appears like that seen on the left of figure 5. Instead, fractures emerge directly from the vent; the dendritic pattern forms as the fractures, which propagate in almost straight lines, repeatedly split into two conduits of

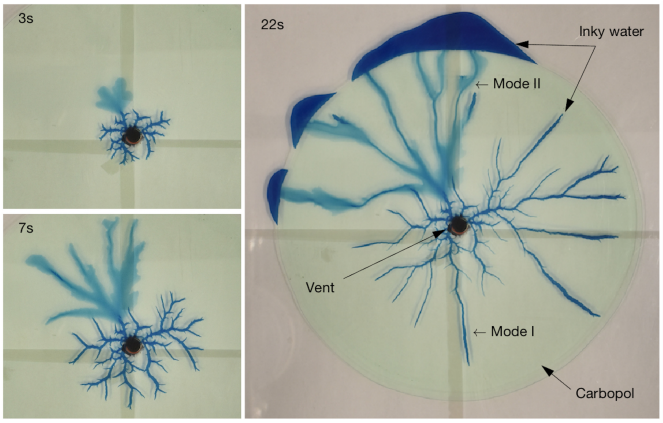

Figure 8: Blue-coloured water pumped into an annulus of (light green) Carbopol in a cell with thickness 1.7mm at pump rate $\mathcal{Q} \simeq 10$ml/min. (Rheology: $n = 0.4$, $\tau_Y = 17$Pa, $K = 9.8$Pa s^n).

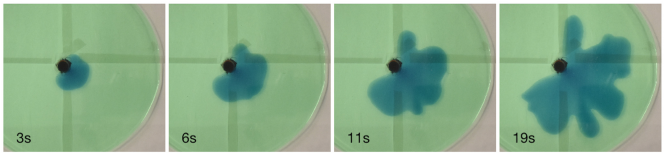

Figure 9: Blue-coloured water pumped into an annulus of (light green) Carbopol in a 4.3mm thick cell at pump rate $\mathcal{Q} \simeq 10$ml/min. (Rheology: $n = 0.4$, $\tau_Y = 17$Pa, $K = 9.8$Pa s^n).

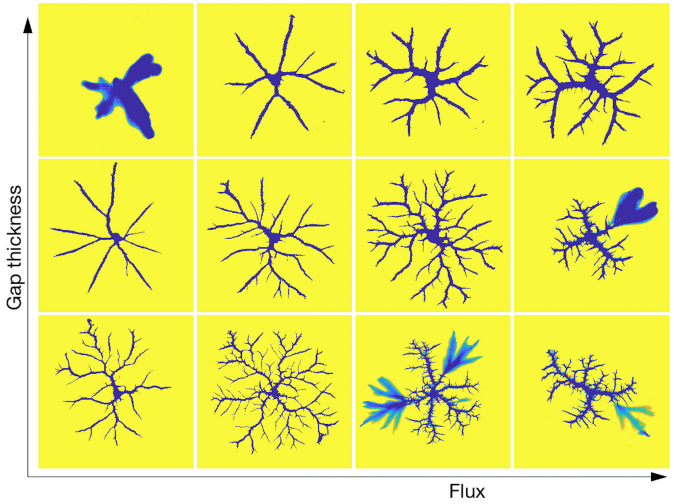

Figure 10: A collage of final fracture patterns for different fluxes (10, 20, 40 and 60 ml/min) and gap thicknesses (1.7, 3.3 and 4.3mm). Pure type-II fracture modes (distinguished by the lighter and broader blue colours) appear in the top left experiment; type-I modes characterize all the others, with the three tests at the bottom right featuring coexisting type-II fractures. (Rheology: $n = 0.4$, $\tau_Y = 17$Pa, $K = 9.8$Pa s^n).

roughly equal size, or spawn multiple smaller side branches without the main conduit changing direction. Overall, the invasive pattern is very different from that in the extraction experiments. The key difference is that the expanding Carbopol annulus is in a state of tension throughout, rather than compression as for the extracted disk. Tear-

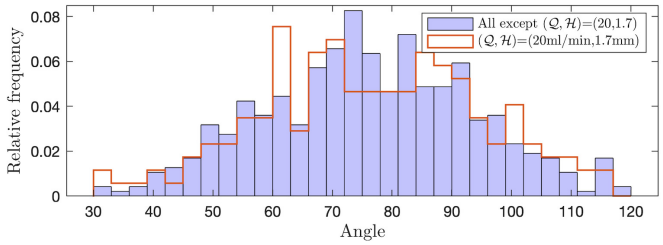

Figure 11: Relative frequency distribution of the angle between split fractures or side branches, showing the experiment with $(\mathcal{Q}, \mathcal{H}) = (20\text{ml/min}, 1.7\text{mm})$ and the data set taken from all the experiments except that particular test.

ing under tension is therefore immediately possible for the expanding annulus, whereas Saffman-Taylor fingering must develop first for the extracted disk to create locally favourable sites along the interface at which to fracture.

Nevertheless, fractures of this type, in which the gel tears across the whole gap of the Hele-Shaw cell, are not the only possibility. The second experiment, shown in figure 8, displays a second phenomenon: initially a dendritic fracture pattern starts to emerge, but then a more diffuse and wider mode of invasion appears that at first sight is more reminiscent of traditional Saffman-Taylor fingers. The new mode is not, however, a fingering displacement, but is actually a different form of fracturing: the Carbopol now fractures off one of the confining plates, rather than internally across the cell, arising either due to the imposed normal or shear stresses there. In other words, a second, boundary mode of fracturing appears. As evident from the images in the figure, the second mode propagates faster than the first one, with the more diffuse conduits reaching the edge of the Carbopol disk first, thereby draining most of the water pumped into the cell.

Although full-gap fractures characterized many of the displacements in our experiments, the wall mode could also emerge by itself. This is illustrated by the final experiment of figure 9, which also corresponds to the cell with the widest gap. In such cases, it is possible that the gel fractures primarily off the wall below the Carbopol once the water is introduced through the feeder pipe attached to the lower plate, before there is time to tear across the entire gap. Aside from such cases, full-gap fractures form earlier than those along the walls, presumably as a result of higher tensile stress concentrations within the gap. A summary of the final fracture patterns in a suite of experiments in which we varied both the pumping rate and cell thickness is shown in figure 10. Mode-I-type fractures (*i.e.* tears across the slot) feature in all but the thickest cells at the lowest fluxes, which exhibit mode-II-type fractures (against the wall). The two fracture modes co-exist at the highest fluxes in the narrower cells. However, additional experiments, not shown in this figure (but see figure 8), also demonstrated that competing fracture modes could arise in the narrower cells at low fluxes, obscuring the conditions favouring each mode. Overall, the number of fractures increases with the flux, due mostly to an enhancement in the frequency at which splittings or side branchings occur, promoting the complexity of the patterns. Another notable feature in figure 10 is that the width of the conduits created by the fractures is relatively insensitive to the flux, but does depend on the gap thickness. All that said, apart from a difference in scale, the patterns are similar along diagonals in the figure.

Measurements of the angles formed when fractures split or side branches appear are shown in figure 11. Each of the tests in figure 10 shows little discernible differences in these angle distributions (the figure compares the measured angles for one of the tests with the corresponding data for all the others), reflecting how the underlying process is insensitive to the flow rate and cell geometry. The distributions show little structure other than a broad peak around 75 degrees and a standard deviation of 20 degrees, over a range from 30 to 120 degrees. This phenomenology is different from that observed in [19] for Hele-Shaw displacement experiments with a colloidal gel, where "visco-elastic" fracture patterns were observed with splitting angles close to 90 degrees.

Additional details of the evolution of the fracture patterns in a subset of the tests (those in the widest cell) are shown in figure 12. Once a fracture appears, the surrounding Carbopol becomes largely arrested, with fluid motion primarily taking place at the fracture tip. The tips of the main fractures advance at roughly constant rate, as seen by the regular spacing of the snapshots of the interface, taken every two seconds. Most of the side branches quickly stop progressing to form dead-ended conduits.

The conduits displayed in figure 12 also maintain a fairly uniform width along their lengths, except at the junctions where the fractures divide. This feature is brought out in more detail in figure 13, which illustrates how conduit widths vary with radial position from the vent for the final patterns of the tests with pure mode-I fractures in figure 10. For simplicity, the widths are extracted by considering the intersections of the fractures with circular arcs (see panel (a)) and so the measured widths are not strictly perpendicular to the conduits. However, the measurements are then averaged over all the fractures to remove any orientation effects, and then plotted against radius (panel (b)). The roughly constant width of the conduit is then evidenced, leading us to take the mean over the radial positions shown in (b). We then plot the result against gap thickness $\mathcal{H}$ in panel (c), bringing out how the conduit width depends on cell geometry (but not flux). In particular, the width appears to be roughly proportional to $\mathcal{H}$, as in immiscible viscous fingering regularized by surface tension (see §2.2.7 and [2]), or miscible viscous fingering and visco-elastic fracture [3, 17] (although the constant of proportionality looks somewhat different, being closer to 4 there), but unlike linear viscoplastic Saffman-Taylor instability (see §2.2.6 and [7, 8]).

If the fractures open up into conduits of constant width proportional to $\mathcal{H}$, the constant flux imposed in the ex-

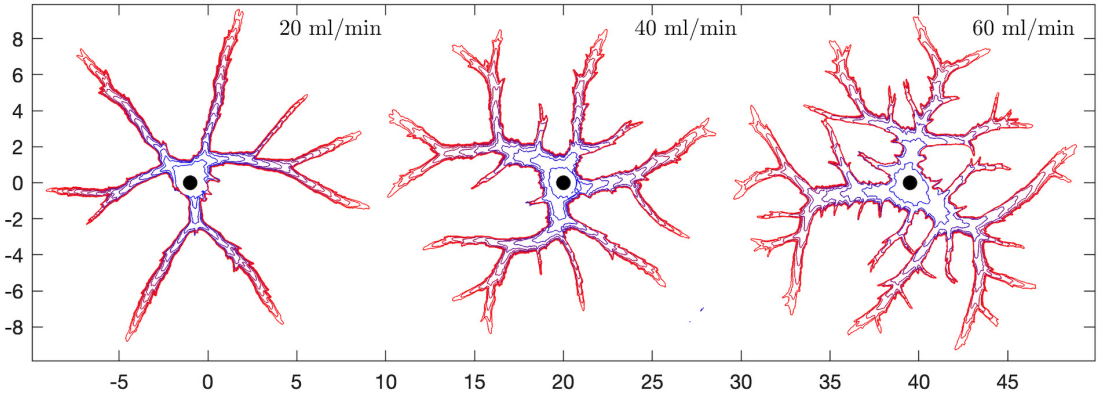

Figure 12: Snapshots of expanding interfaces every 2 seconds in the slot of thickness 4.3mm with the fluxes shown, and colour coded by time (with distance measured in cm). (Rheology: $n = 0.4$, $\tau_Y = 17$Pa, $K = 9.8$Pa s^n).

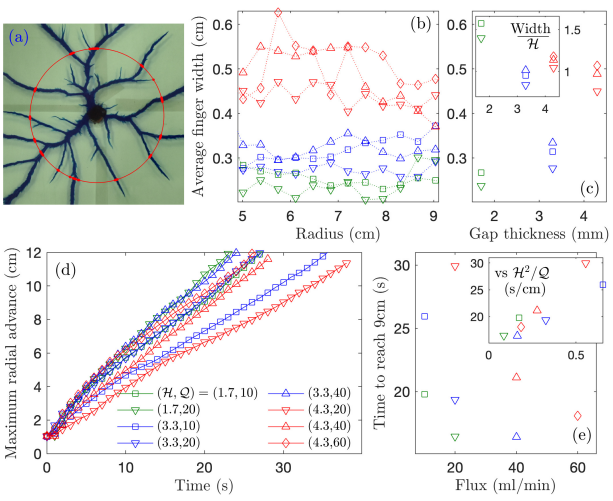

Figure 13: Measurements of conduit width for the final patterns of the tests in figure 10 with pure mode-I fractures. These are extracted by considering the intersection of the fractures with circular arcs (discounting conduits less than about 0.2mm wide; panel (a)). The average width over all the fractures is plotted against radial position from the vent in (b), and then averaged again over radius and plotted against gap thickness in (c). The inset of (c) replots the data, scaling the averaged width by gap thickness $\mathcal{H}$. In (d), we show the maximum radial advance of the fractures against time for the various tests. The symbol convention used to plot all the data is shown by the legend in this panel. Finally, in (e), we plot the time taken for the fractures to first reach a radius of 9cm against the flux; the inset replots this data against $\mathcal{H}^2/\mathcal{Q}$.

periments demands that the tips must advance linearly in time, as suggested by the uniformly spaced interface snapshots of figure 12. Further evidence for this feature (save for a short transient at early times, and a final phase where the fractures approach the outer edge of the Carbopol) is shown in figure 13(d), which plots the maximum radial extent of the fracture pattern against time. The time required for the pattern to reach a fixed radial position should therefore depend on the combination $\mathcal{H}^2/\mathcal{Q}$, as seen in panel (e), in which the data for the time to reach a fixed radial position are largely collapsed.

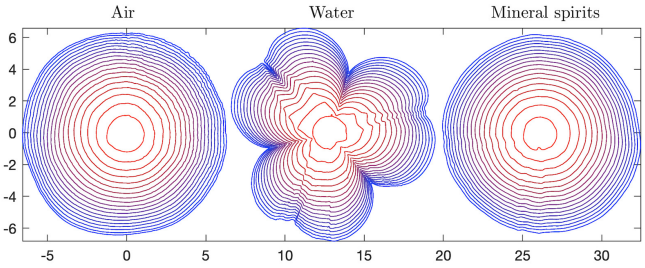

Figure 14: Carbopol (with yield stress 12Pa) pumped with rate $\mathcal{Q} \simeq$ 10ml/min into a $\mathcal{H} = 4.3$mm cell filled with the Newtonian fluids indicated. Shown are snapshots of the interface, equally spaced and coloured by time (with distance measured in cm).

3.2.3. For an interface stable against Saffman-Taylor

Finally, we consider the problem in which we pump Carbopol into a Hele-Shaw cell displacing a Newtonian fluid. The Saffman-Taylor instability is not expected to operate in this setting, and indeed the interface expands axisymmetrically when the cell is filled with either air or an immiscible Newtonian fluid of similar viscosity to that of water; see figure 14. Nevertheless, the interface is now in a state of expansion, and therefore tension, which potentially sets the stage for fractures to appear. Indeed, when the gap is filled by water, as shown by the examples in figures 14 and 15, cracks spanning the cell appear at the interface. These features destroy the axisymmetry of the interface, but remain relatively localized and expand in step with the interface. This results in relatively weak pattern of instability. Note that, in these experiments, to ensure that the interface was circular at the outset of the test, we first pumped a small amount of Carbopol into an empty cell (to a radius of about a centimetre), then poured the water into the rest of the cell around the emplaced disk. We also used suspensions with a wider range of Carbopol concentrations; table 1 lists the parameters of the Herschel-Bulkley fits (we use the yield stress as a convenient label for each).

As illustrated in figures 16 and 17, the degree of non-

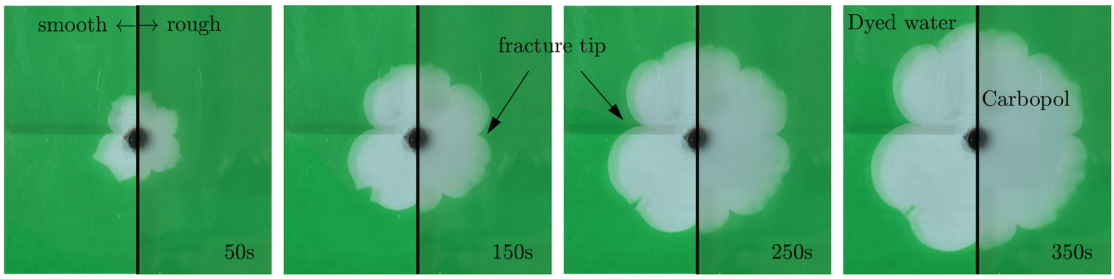

Figure 15: Carbopol (with yield stress 12Pa) pumped into water in a 4.3mm thick cell at pump rate $\mathcal{Q} \simeq 10$ml/min. On the left of each snapshot, the cell has smooth plexiglass walls; on the right, the walls have been roughened with 60-grit sandpaper.

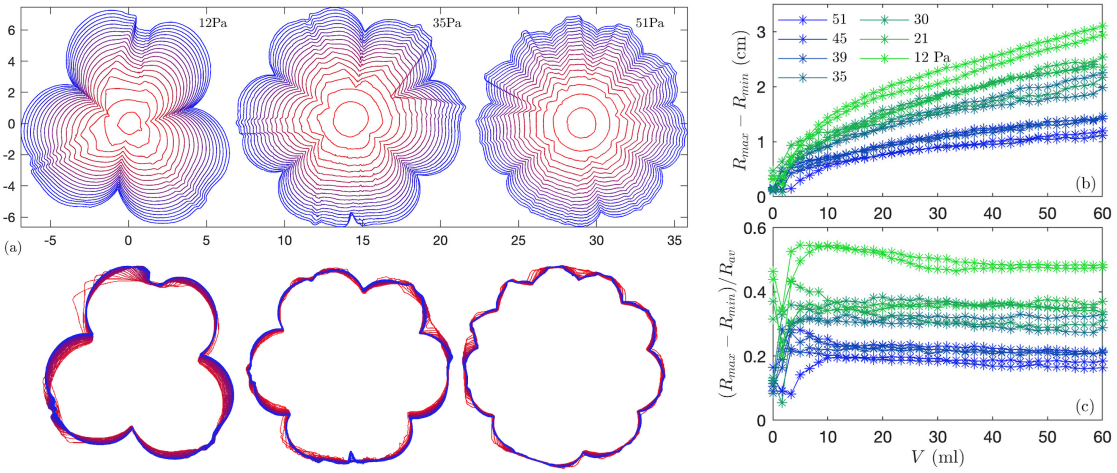

Figure 16: Carbopol with the yield stresses indicated pumped into a 4.3mm thick cell at pump rate $\mathcal{Q} \simeq 10$ml/min. (a) shows snapshots of the interface, equally spaced and coloured by time (with distance measured in cm); the lower plots show the interfaces rescaled by the maximum radius, eliminating the first few to remove the initial transient. On the right, we plot (b) the difference in maximum and minimum radii $R_{max} - R_{min}$ and (c) the scaled difference $(R_{max} - R_{min})/R_{av}$, all colour coded by τ_Y.

axisymmetry in the fracture pattern depends on the Carbopol concentration and flux. To quantify this feature, we observe that the difference between the maximum and minimum radii, R_{max} and R_{min}, scales approximately with $R_{av} = \sqrt{r_v^2 + \mathcal{Q}t/(\pi\mathcal{H})}$ after an initial transient (figure 16(b-c)). Thus we formulate the average $\langle (R_{max} - R_{min})/R_{av} \rangle$, for volumes over the range, $10 < V < 60$ml. This diagnostic is plotted against τ_Y and $\mathcal{Q}$ in figure 18; additional experiments in cells with different gap width are also shown. Evidently, the implied strength of the pattern decreases with yield stress and flux, and increases with the gap thickness. The scaling of R_{max} and R_{min} with R_{av} suggests that the fracture patterns may evolve into a self-similar form; some additional evidence for this is provided in figures 16 and 17, which replots the snapshots of the interface after scaling distance by the maximum radius.

Figure 18 also plots the number of clearly identifiable fractures at the end of the tests, which indicates the typical spacing of these features given that a comparable amount of Carbopol was pumped into the cell each time. The fracture spacing is not very sensitive to the Carbopol concentration, but certainly decreases as the flux is increased or the gap reduced (*cf.* figures 16 and 17; note that the smaller corrugations evident in the first set of interfaces in figure 17 are not the result of independent fractures, but are the corners of the four primary cracks that become swept sideways by the radial expansion).

A more insidious effect is provided by the plates of the cell themselves: for the most part we used smooth plexiglass for the cell. However, in view of the likely presence of wall slip, we also performed tests with plates that were roughened with sandpaper to reduce any effective sliding. A comparison between tests in smooth and roughened cells is shown in figure 15. The cracks spanning the smooth cell open further in radius and are more numerous around the interface. This suggests that there is an additional containment effect for roughened walls, limiting the development of the fractures, that perhaps results from the elimination of wall slip.

One interesting feature brought out by the plots of the interface at successive instants in figures 16 and 17 is the fractures sometimes isolate almost straight pieces of the interface that become advected out radially without any change of shape. As these sections, and the adjoining, apparently unyielded material, separate from one another under the radial expansion, fresh fluid flows into the gaps, creating distinctive, petal-like structures. The relatively regular spacing of the fracture then lends a flower-like ap-

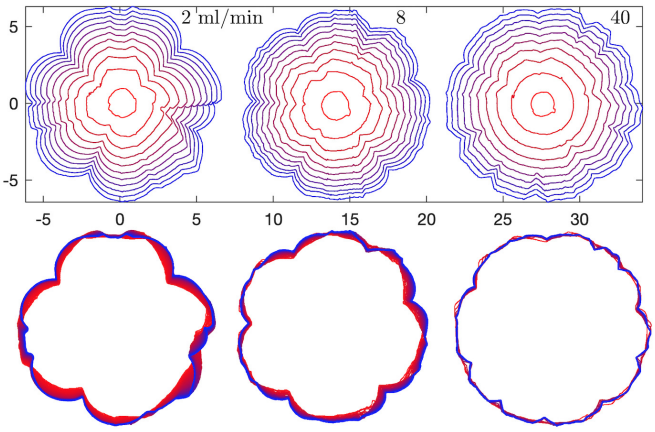

Figure 17: Carbopol with yield stress 51Pa pumped into a 4.3mm thick cell at the fluxes indicated. Shown are snapshots of the interface, equally spaced in the amount of pumped fluid, and coloured by time (with distance measured in cm); the lower plots show the interfaces rescaled by the maximum radius, eliminating the first few to remove the initial transient.

τ_Y (Pa)	51	45	39	35	30	21	12
K (Pa s^n)	29	25	24	23	20	12	9
n	0.38	0.38	0.37	0.36	0.36	0.39	0.39

Table 1: Herschel-Bulkley fits for the different Carbopol concentrations used in the tests of §3.2.3.

pearance to the fracture pattern.

We close by briefly comparing the Carbopol tests with an experiment with a different viscoplastic fluid: joint compound (a commercially available, kaolin-based material) diluted with water to a concentration where the yield stress is about 50 Pa. Pumping this fluid into an empty Hele-Shaw cell again generates a smooth, axisymmetrically expanding interface. But with water in the cell, the interface rapidly develops a fracture pattern somewhat like in the Carbopol tests; see figure 19. However, for this material the interface appears to have very little integrity, breaking up due to the creation of many fine cracks and developing a rougher appearance. Larger V-shaped cracks subsequently develop from some of the fine structure, giving the pattern another flower-like shape. Again, there is evidence for self-similarity: the last images on the right of figure 19 are plotted with an expanding scale (as evidence from the grid on the paper backing to the cell).

Note that the opacity of the joint compound permits us to look for any residual layers of (dyed) water attached to the walls of the cell left behind by the displacing viscoplastic fluid. Such observations do indeed reveal thin layers of water buffering the cell wall near the advancing interface. However, these layers are not wide, implying the joint compound largely displaces the water from the surface. Tests in which Carbopol displaced dark ink showed the same feature. Thus, there appears to be little additional lubrication of the viscoplastic fluids at the plates due to residual wall layers of water.

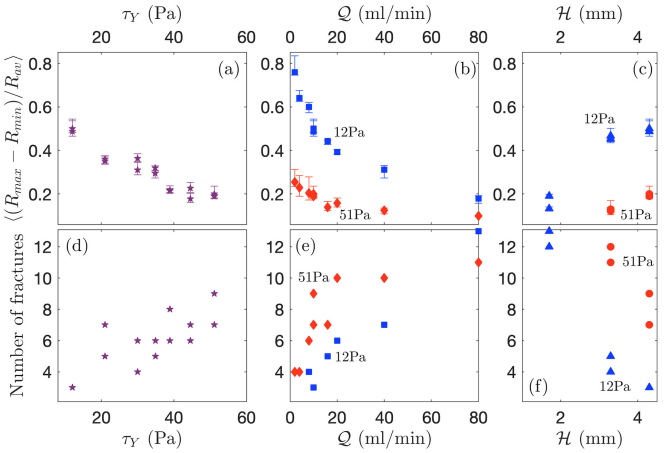

Figure 18: The average scaled radial difference, $\langle (R_{max} - R_{min})/R_{av} \rangle$, for $10 < V < 60$ml, and number of fractures plotted against (a) τ_Y (for $\mathcal{Q} \simeq 10$ml/min, $\mathcal{H} = 4.3$mm), (b) $\mathcal{Q}$ (for $\tau_Y = 12, 51$Pa, $\mathcal{H} = 4.3$ mm) and (c) $\mathcal{H}$ (for $\mathcal{Q} \simeq 10$ml/min, $\tau_Y = 12, 51$Pa). The error bars in (a-c) correspond to the maximum and minimum values of the non-axisymmetry measure over volumes $10 < V < 60$ml.

4. Discussion

In this paper, we have summarized the theoretical analysis of the classical Saffman-Taylor fingering, as modified by a yield stress and examined previously by Coussot [7]. In this case, we delved into further details of the stability problem, considering the two radial displacement problems illustrated in figure 1. The interface bordering a viscoplastic fluid is stable if advancing into a low-viscosity Newtonian fluid, but unstable if retreating. The instability is exacerbated by the yield stress, which raises the effective viscosity contrast across the interface. Our analysis incorporates the time dependence of the base state by solving the linear initial-value problem, thereby accounting for the evolving impact of surface tension and identifying the most unstable angular modes.

In Appendix A, we provide further theoretical discussion of another flow instability that might be relevant in a Hele-Shaw cell if the viscoplastic fluid suffers substantial wall slip over the plates. In this situation, the flow may become almost two dimensional, bringing up the possibility that a recently discovered instability of shear-thinning power-law fluids in radial extensional flow [24, 25] may activate non-axisymmetrical patterns. In Appendix A, we generalize the theoretical discussion of this instability to Herschel-Bulkley fluids. Although we find that the instability is still present with a yield stress, it seems unlikely to be sufficiently strong to become prominent in a Hele-Shaw cell.

Our theoretical discussion complements a variety of laboratory experiments conducted with aqueous suspensions of Carbopol displacing or displaced by either air, water or oil. The viscoplastic version of the Saffman-Taylor instability is observed when air is pumped into a cell filled with Carbopol, or when a disk of Carbopol emplaced in the cell

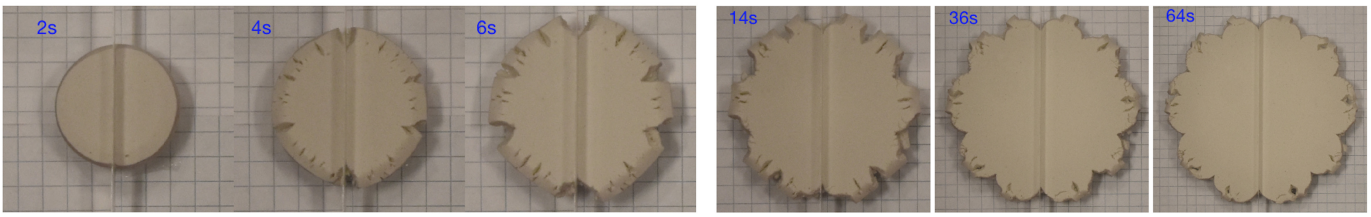

Figure 19: Joint compound with a yield stress of around 50 Pa. On the left, the images have the same scale; on the right, the images are cropped to bring out the structure of the edge and self-similar evolution (the scale can be judged from the size of the grid on the paper backing to the cell).

is withdrawn. For the former experiments, theoretical predictions appear to be in fair agreement with experimental observations: the most unstable angular wavenumber is roughly consistent with the patterns observed (assuming interfacial tensions to be comparable to the surface tension of water). Curiously, for the extraction problem, the comparison is less satisfying, with the linear stability theory predicting higher wavenumbers that seen experimentally. Similar discrepancies were observed by Derks *et al.* [14] in plate-separation experiments.

Both experiments show dramatic differences when performed with water as the second fluid: in the extraction experiment, a similar viscoplastic Saffman-Taylor instability is observed initially. Although the angular wavenumbers are slightly higher than for air displacement, they are not significantly so, which is surprising in view of the fact that the two fluids are now miscible. Interfacial tension effects are therefore minimal, and so the most unstable wavelengths are expected to scale down to the thickness of the cell [3]. This surprise is compounded by a secondary instability that appears when the finger pattern has developed sufficiently to create concave sections of the interface. The tension generated over these pieces of the interface then causes the Carbopol to fracture; the cracks rapidly propagate in an almost angular direction, severing fingers and disfiguring the pattern.

In the experiments in which water is pumped into a Carbopol-filled cell, the entire expanding interface is under tension and the fractures form immediately, supplanting any Saffman-Taylor fingering. Dendritic fracture patterns then advance rapidly into the cell. Two types of fractures are observed: the most common consist of cracks across the cell, but a second variety can also appear in which the Carbopol fractures off the cell walls.

The fractures do not occur when other immiscible fluids are used instead of water, with Saffman-Taylor fingers appearing much like in the air displacement experiments. Also, the fractures are not sensitive to whether the water was distilled, taken directly from a tap, or coloured with ink. We further added sugar to raise the viscosity by up to a factor of about ten (and potentially change the interfacial interaction with the Carbopol), with no qualitative effect on the fracturing and a minimal quantitative one. The experiments therefore clearly distinguish Saffman-Taylor fingering from fracture patterns, and suggest the main property of the second fluid that is required for the latter is that it is water-based.

When Carbopol was pumped into a cell filled with either air or an immiscible oil, the interface remained axisymmetrical, indicating that no shear-thinning extensional flow instability of the kind explored in Appendix A operates in this configuration. Once more, however, pumping Carbopol into a water-filled cell can lead to non-axisymmetrical patterns. We identified the culprit to again be the fracturing of the expanding interface under tension. In this setting the fractures do not develop strongly but remain localized close to the interface, becoming effectively contained by the yield stress of the fluid, the narrow gap and the inability to slide freely over the cell walls.

Finally, it has been pointed out that the Saffman-Taylor instability can be critically affected by the wettability properties of the two fluids participating in the displacement [12, 31, 32]. Such effects do not appear to play any role in our experiments, as illustrated by our displacements involving either air or oil: these two fluids are expected to wet the plates very differently at their interface with Carbopol. However no qualitative differences were observed.

Acknowledgements We thank Mark Martinez, Stephen Morris, Roiy Sayag and Grae Worster for useful discussions.

Declaration of Competing Interest We declare no conflict of interests.

Appendix A. Two-dimensional viscoplastic, extensional flow instability

Consider a two-dimensional Herschel-Bulkley fluid flowing out from a source with flux $\mathcal{Q}$ and radius r_v. We again write the governing equations in dimensionless form, using a similar scaling of the governing fluids equations to §2, except we scale the stress by $K(\mathcal{V}/\mathcal{L})^n$. Then, ignoring inertia, force balance and incompressibility demand

$$p_r = \frac{1}{r^2}\frac{\partial}{\partial r}(r^2\tau_{\mathrm{r}\mathrm{r}}) + \frac{1}{r}\frac{\partial \tau_{\mathrm{r}\theta}}{\partial \vartheta}, \tag{A.1}$$

$$p_\vartheta = \frac{1}{r}\frac{\partial}{\partial r}(r^2\tau_{\mathrm{r}\theta}) + \frac{\partial \tau_{\theta\theta}}{\partial \vartheta} \tag{A.2}$$

and

$$(ru)_r + v_\vartheta = 0, \tag{A.3}$$

where p and $\{\tau_{rr}, \tau_{r\theta}, \tau_{\theta\theta}\}$ denote the pressure and deviatoric stress components, (u, v) is the velocity field, and the (t, r, ϑ) subscripts are a shorthand notation for partial derivatives. Assuming that the fluid always remains yielded as it is driven through the cell (demanding ${\tau_{rr}}^2 + {\tau_{r\theta}}^2 > \mathrm{Bi}^2$), the constitutive law can be written as

$$[\tau_{rr}, \tau_{r\theta}] = \left(\dot{\gamma}^{n-1} + \frac{\mathrm{Bi}}{\dot{\gamma}}\right)[2u_r, (u_\vartheta - v)/r + v_r], \quad \text{(A.4)}$$

where

$$\dot{\gamma} = \sqrt{4u_r^2 + [(u_\vartheta - v)/r + v_r]^2} \quad \text{(A.5)}$$

and the Bingham number is

$$\mathrm{Bi} = \frac{\tau_Y \mathcal{L}^n}{K\mathcal{V}^n}. \quad \text{(A.6)}$$

The outer radius of the fluid is given by $r = R(\vartheta, t)$. Here, the kinematic and stress conditions demand

$$R_t + \frac{v}{R}R_\vartheta = u, \quad \text{(A.7)}$$

$$\left(1 + \frac{R_\vartheta^2}{R^2}\right)p - \left(1 - \frac{R_\vartheta^2}{R^2}\right)\tau_{rr} + 2\frac{R_\vartheta}{R}\tau_{r\theta} = 0 \quad \text{(A.8)}$$

and

$$\left(1 - \frac{R_\vartheta^2}{R^2}\right)\tau_{r\theta} + 2\frac{R_\vartheta}{R}\tau_{rr} = 0, \quad \text{(A.9)}$$

in the absence of any interfacial tension or forces exerted by the adjacent fluid.

When the flow remains axisymmetrical, a base outflow is established with

$$u = \frac{1}{r}, \quad R = \sqrt{1 + 2t}, \quad \dot{\gamma} = \frac{2}{r^2}, \qquad \tau_{rr} = -\mathrm{Bi} - \frac{2^n}{r^{2n}}, \quad \text{(A.10)}$$

$$p = 2\mathrm{Bi}\ln\left(\frac{R}{r}\right) - \mathrm{Bi} + \frac{2^n}{n}(1-n)r^{-2n} - \frac{2^n}{n}R^{-2n}. \quad \text{(A.11)}$$

Along the lines summarized by Sayag & Worster, we may analyze the linear stability of this state towards non-axisymmetrical disturbances with azimuthal wavenumber m. The perturbations to the solution in (A.10)–(A.11), which we denote by adding a hat decoration and with dependence $e^{im\vartheta}$, satisfy the relations,

$$\begin{gathered}
\frac{\partial}{\partial r}(\hat{\tau}_{rr} - \hat{p}) + \frac{2}{r}\hat{\tau}_{rr} + \frac{1}{r}\frac{\partial \hat{\tau}_{r\theta}}{\partial \vartheta} = 0, \\
\frac{\partial}{\partial r}\left(r^2\frac{\partial \hat{\tau}_{r\theta}}{\partial \vartheta}\right) + m^2 r(\hat{\tau}_{rr} + \hat{p}) = 0, \\
\hat{u}_r + \frac{1}{r}\hat{u} + \frac{\hat{v}_\vartheta}{r} = 0, \\
\left(\frac{\hat{v}_\vartheta}{r}\right)_r - \frac{1}{r\mu}\frac{\partial \hat{\tau}_{r\theta}}{\partial \vartheta} - \frac{m^2}{r^2}\hat{u} = 0,
\end{gathered} \quad \text{(A.12)}$$

with

$$\mu = 2^{n-1}r^{2-2n} + \tfrac{1}{2}r^2\mathrm{Bi}, \qquad \hat{\tau}_{rr} = -2^n n r^{1-2n}\left(\hat{u} + r\frac{\hat{v}_\vartheta}{r}\right). \quad \text{(A.13)}$$

The boundary conditions are $\hat{u}(1, \vartheta, t) = \hat{v}_\vartheta(1, \vartheta, t) = 0$ (fixed inflow at the vent), and

$$\hat{\tau}_{rr} - \hat{p} + \frac{2}{r}\hat{R}\left(\frac{2^n}{r^{2n}} + \mathrm{Bi}\right) = 0 \quad \text{(A.14)}$$

and

$$r\frac{\partial \hat{\tau}_{r\theta}}{\partial \vartheta} + 2m^2\hat{R}\left(\frac{2^n}{r^{2n}} + \mathrm{Bi}\right) = 0 \quad \text{(A.15)}$$

at $r = \sqrt{1 + 2t}$ (the unperturbed outer radius).

As in conventional Stokes problems, the system dynamics enters only through the motion of the boundary; *i.e.* the interface $r = R(\vartheta, t) \to \sqrt{1 + 2t} + \hat{R}(t)e^{im\vartheta}$. The equations for the linear perturbations can therefore be solved as a spatial problem at each moment in time, with the solution being proportional to $\hat{R}(t)$. The result can then be fed into the kinematic condition, $\hat{R}_t = \hat{u}$, to define an instantaneous growth rate $G(t) = \hat{R}_t/\hat{R}$. Evidently,

$$\hat{R}(t) = \hat{R}(0)\exp\left[\int_0^t G(\hat{t})\mathrm{d}\hat{t}\right] \equiv A(t)\hat{R}(0), \quad \text{(A.16)}$$

where the amplification factor $A(t)$ can be evaluated at some nominal time to furnish a convenient measure of the strength of instability.

Figure A.20 displays numerical solutions to the linear stability problem for $m = 2$, 3, ..., 10, using the rheological parameter settings $n = 0.4$ and $\mathrm{Bi} = 0$ or 1 (such values are guided by the experiments conducted in §3, which use a Carbopol solution with that shear-thinning exponent and operating conditions corresponding to $\mathrm{Bi} = O(1)$). As found by Sayag & Worster, each azimuthal wavenumber passes through an interval over which the instantaneous growth rate is positive, implying mode growth. However, as indicated by the growth factor $A(t)$, for $\mathrm{Bi} = 0$ the actual degree of amplification is small, with only the $m = 2$ mode amplifying above the initial value over its window of instability, and damping over longer times suppressing every mode. Modes grow slightly more significantly with $\mathrm{Bi} = 1$, although the overall picture is much the same. This is emphasized further in figure A.21, which shows the maximum possible amplification factor for a selection of modes as a function of Bi. Note that, as observed by Sayag & Worster, the instantaneous growth rate $G(t)$ collapses to a common form for the higher-order modes ($m \gg 1$) when plotted against mt, implying significant limitations on the corresponding amplification factor $A(t)$.

At least with these choices for the rheological parameters, the extensional flow instability therefore seems rather weak, particularly in the limit of a power-law fluid ($\mathrm{Bi} = 0$). The inclusion of surface tension likely suppresses the instability yet further, especially at high wavenumber. The $m = 1$ mode is, however, different: this mode remains unstable over a relatively long interval (see figure A.22), sufficient to permit a substantial amount of amplification. Nevertheless, as this mode corresponds mostly to a sideways shift of the expanding fluid column, the instability

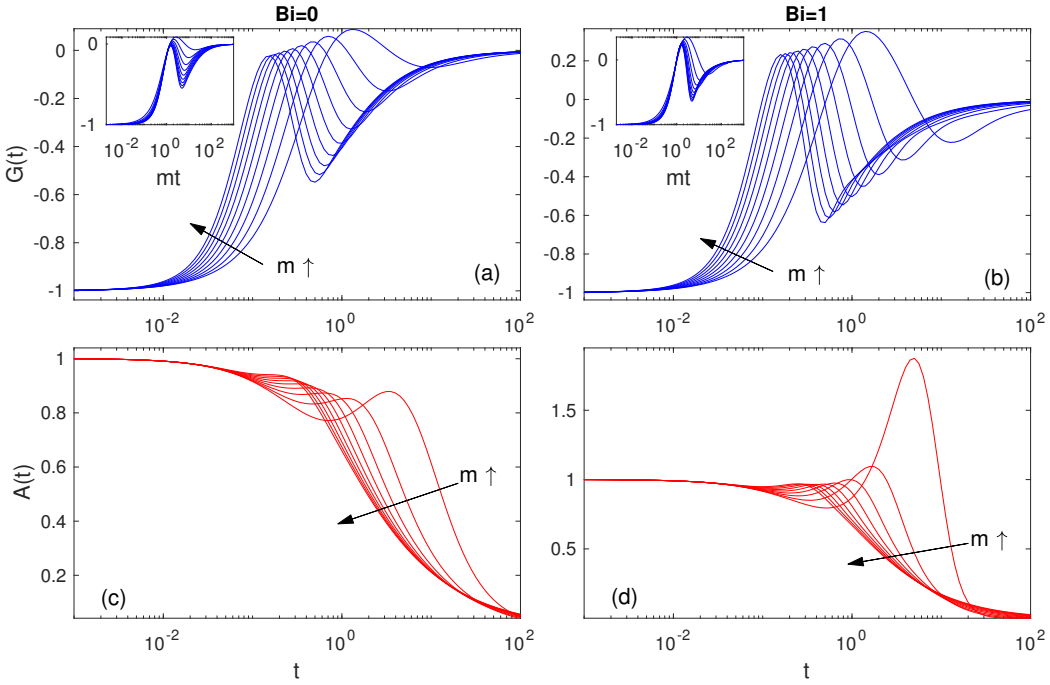

Figure A.20: Instantaneous (a,b) growth rates $G(t)$ and (c,d) amplification factors $A(t)$ for $m = 2$, 3, 4 ..., 10 and $\mathrm{Bi} = 0$ (a,c) and $\mathrm{Bi} = 1$ (b,d); $n = 0.4$. The insets in (a,b) replot the data for $G(t)$ against mt, which aligns the windows of instability (Sayag & Worster).

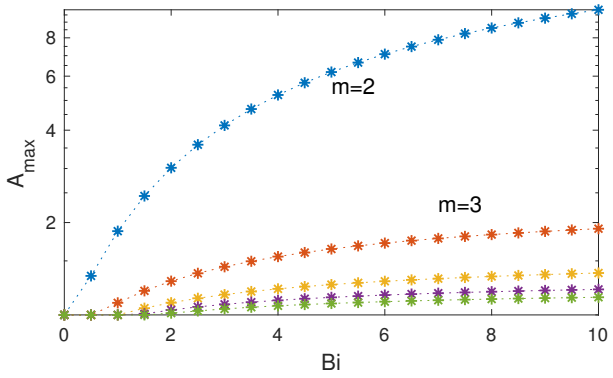

Figure A.21: Maximum amplification factors A_{max} over $0 < t < 100$ against Bi for $m = 2$, 3, ..., 6. ($n = 0.4$)

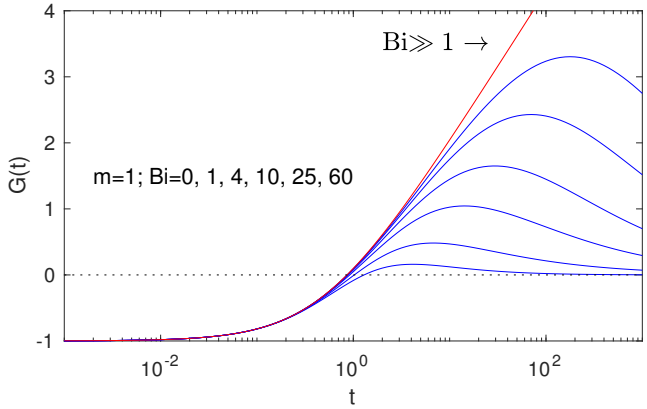

Figure A.22: Instantaneous growth rates for the $m = 1$ mode with the values of Bi indicated, as well as the $\mathrm{Bi} \gg 1$ limit. ($n = 0.4$)

is not expected to generate a pattern with the form of multiple "fingers".

For large yield stress ($\mathrm{Bi} \gg 1$), we may solve the linear stability problem analytically: from (A.13) we observe that $\hat{\tau}_{rr}$ remains $O(1)$, whilst $\hat{p}$ and $\hat{\tau}_{r\theta}$ must both become $O(\mathrm{Bi})$ in order to balance the largest terms in (A.12) and (A.15). Thus, the first two relations in (A.12) decouple from the others and imply that

$$\hat{p} \sim \frac{2}{r}\mathrm{Bi}(\cos\Theta + \Gamma\sin\Theta) \qquad \& \qquad \frac{\partial\hat{\tau}_{r\theta}}{\partial\vartheta} \sim -\frac{2}{r}m^2\mathrm{Bi}\cos\Theta, \tag{A.17}$$

in view of the leading-order boundary conditions, where

$$\Theta = \Gamma\log\frac{\sqrt{1+2t}}{r}, \qquad \Gamma = \sqrt{m^2-1}. \tag{A.18}$$

These relations can be substituted back into the remainder of (A.12) and (A.13) to find $\hat{u}$. After a little algebra, the kinematic condition then furnishes the handy result,

$$\hat{R}^{-1}\frac{d\hat{R}}{dt} = G(t) \sim \frac{1}{\Gamma}\sin[\Gamma\log(1+2t)] - \cos[\Gamma\log(1+2t)]. \tag{A.19}$$

For $m \gg 1$ and $t \ll 1$, we find $G \to -\cos(2mt)$, which is analogous to a result provided by Sayag & Worster in the limit $n \ll 1$ for a power-law fluid. However, the result in (A.19) applies for all wavenumbers and times. The progress of numerically computed growth rates to the $\mathrm{Bi} \gg 1$ limit is illustrated in figure A.23 for modes with $m = 4$. The limit in (A.19) has a curious oscillatory structure, explored in detail by Sayag & Worster. The repeated intervals with positive growth rate highlight how the instability is potentially more powerful in the perfectly plastic

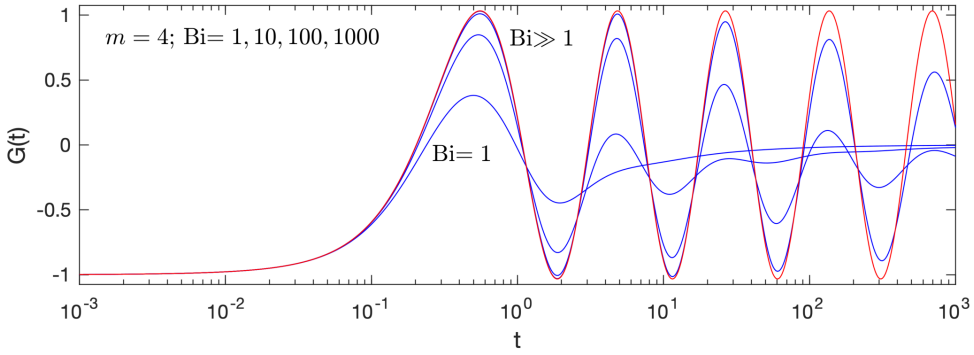

Figure A.23: Instantaneous growth rates for the $m = 4$ mode with the values of Bi indicated. The (red) line marked Bi $\gg 1$ shows the prediction (A.19). ($n = 0.4$)

limit. Nevertheless, the $m = 1$ mode still dominates over longer times, with the growth rate actually growing logarithmically with t: $G(t) \sim \log(1 + 2t) - 1$ (*cf.* figure A.22).

In summary, we have generalized the linear stability theory for extensional flow of two-dimensional shear-thinning fluids to the Herschel-Bulkley model, thereby incorporating a yield stress and examining the perfectly plastic limit. In general, the instability appears to be relatively weak, with exception of the $m = 1$ model where substantial amplification is possible. This mode corresponds to a sideways shift of the expanding cylinder and is unlikely to create multiple fingers.

[1] P. G. Saffman, G. I. Taylor, The penetration of a fluid into a porous medium or Hele-Shaw cell containing a more viscous liquid, Proceedings of the Royal Society of London. Series A. Mathematical and Physical Sciences 245 (1242) (1958) 312–329.

[2] L. Paterson, Radial fingering in a Hele-Shaw cell, Journal of Fluid Mechanics 113 (1981) 513–529.

[3] L. Paterson, Fingering with miscible fluids in a Hele-Shaw cell, The Physics of fluids 28 (1) (1985) 26–30.

[4] S. D. R. Wilson, A note on the measurement of dynamic contact angles, Journal of Colloid and Interface Science 51 (3) (1975) 532–534.

[5] S. D. R. Wilson, The Taylor–Saffman problem for a non-Newtonian liquid, Journal of Fluid Mechanics 220 (1990) 413–425.

[6] L. Kondic, M. J. Shelley, P. Palffy-Muhoray, Non-Newtonian Hele-Shaw flow and the Saffman-Taylor instability, Physical Review Letters 80 (7) (1998) 1433.

[7] P. Coussot, Saffman–Taylor instability in yield-stress fluids, Journal of Fluid Mechanics 380 (1999) 363–376.

[8] A. Lindner, P. Coussot, D. Bonn, Viscous fingering in a yield stress fluid, Physical Review Letters 85 (2) (2000) 314.

[9] N. Maleki-Jirsaraei, A. Lindner, S. Rouhani, D. Bonn, Saffman–Taylor instability in yield stress fluids, Journal of Physics: Condensed Matter 17 (14) (2005) S1219.

[10] O. A. Fadoul, P. Coussot, Saffman–Taylor instability in yield stress fluids: Theory–experiment comparison, Fluids 4 (1) (2019) 53.

[11] J. V. Fontana, S. A. Lira, J. A. Miranda, Radial viscous fingering in yield stress fluids: Onset of pattern formation, Physical Review E 87 (1) (2013) 013016.

[12] A. Eslami, S. M. Taghavi, Viscous fingering of yield stress fluids: The effects of wettability, Journal of Non-Newtonian Fluid Mechanics 264 (2019) 25–47.

[13] B. Ebrahimi, P. Mostaghimi, H. Gholamian, K. Sadeghy, Viscous fingering in yield stress fluids: a numerical study, Journal of Engineering Mathematics 97 (1) (2016) 161–176.

[14] D. Derks, A. Lindner, C. Creton, D. Bonn, Cohesive failure of thin layers of soft model adhesives under tension, Journal of applied physics 93 (3) (2003) 1557–1566.

[15] Q. Barral, G. Ovarlez, X. Chateau, J. Boujlel, B. Rabideau, P. Coussot, Adhesion of yield stress fluids, Soft Matter 6 (6) (2010) 1343–1351.

[16] T. Divoux, A. Shukla, B. Marsit, Y. Kaloga, I. Bischofberger, Criterion for fingering instabilities in colloidal gels, Physical Review Letters 124 (1) (2020) 248006.

[17] H. Van Damme, C. Laroche, L. Gatineau, P. Levitz, Viscoelastic effects in fingering between miscible fluids, Journal de Physique 48 (7) (1987) 1121–1133.

[18] H. Van Damme, C. Laroche, L. Gatineau, Radial fingering in viscoelastic media, an experimental study, Revue de physique appliquée 22 (4) (1987) 241–252.

[19] E. Lemaire, P. Levitz, G. Daccord, H. Van Damme, From viscous fingering to viscoelastic fracturing in colloidal fluids, Physical review letters 67 (15) (1991) 2009.

[20] H. Zhao, J. V. Maher, Associating-polymer effects in a Hele-Shaw experiment, Physical Review E 47 (6) (1993) 4278.

[21] T. Baumberger, C. Caroli, D. Martina, Solvent control of crack dynamics in a reversible hydrogel, Nature materials 5 (7) (2006) 552–555.

[22] T. Baumberger, C. Caroli, D. Martina, Fracture of a biopolymer gel as a viscoplastic disentanglement process, The European Physical Journal E 21 (1) (2006) 81–89.

[23] T. Baumberger, O. Ronsin, A convective instability mechanism for quasistatic crack branching in a hydrogel, The European Physical Journal E 31 (1) (2010) 51–58.

[24] R. Sayag, M. G. Worster, Instability of radially spreading extensional flows. Part 1: Experimental analysis, Journal of Fluid Mechanics 881 (2019) 722–738.

[25] R. Sayag, M. G. Worster, Instability of radially spreading extensional flows. Part 2: Theoretical analysis, Journal of Fluid Mechanics 881 (2019) 739–771.

[26] H. A. Barnes, A review of the slip (wall depletion) of polymer solutions, emulsions and particle suspensions in viscometers: its cause, character, and cure, Journal of Non-Newtonian Fluid Mechanics 56 (3) (1995) 221–251.

[27] Y. Liu, N. J. Balmforth, S. Hormozi, Axisymmetric viscoplastic dambreaks and the slump test, Journal of Non-Newtonian Fluid Mechanics 258 (2018) 45–57.

[28] M. Daneshi, J. MacKenzie, N. J. Balmforth, D. M. Martinez, D. R. Hewitt, Obstructed viscoplastic flow in a hele-shaw cell, Physical Review Fluids 5 (1) (2020) 013301.

[29] D. R. Hewitt, M. Daneshi, N. J. Balmforth, D. M. Martinez, Obstructed and channelized viscoplastic flow in a Hele-Shaw cell, Journal of Fluid Mechanics 790 (2016) 173–204.

[30] S. S. Cardoso, A. W. Woods, The formation of drops through viscous instability, Journal of Fluid Mechanics 289 (1995) 351–

378.
[31] B. Levaché, D. Bartolo, Revisiting the saffman-taylor experiment: imbibition patterns and liquid-entrainment transitions, Physical review letters 113 (4) (2014) 044501.
[32] B. Zhao, C. W. MacMinn, R. Juanes, Wettability control on multiphase flow in patterned microfluidics, Proceedings of the National Academy of Sciences 113 (37) (2016) 10251–10256.